Inorganic Chemistry
Article
pubs.acs.org/IC

QM/MM Structural and Spectroscopic Analysis of the Di-iron(II) and Di-iron(III) Ferroxidase Site in M Ferritin

Travis V. Harris and Keiji Morokuma*

Fukui Institute for Fundamental Chemistry, Kyoto University, Kyoto 606-8103, Japan

Supporting Information

ABSTRACT: Ferritins are cage-like proteins composed of 24 subunits that take up iron(II) and store it as an iron(III) oxide mineral core. A critical step is the ferroxidase reaction, in which oxygen reacts with a di-iron(II) site, proceeding through a peroxo intermediate, to form μ-oxo/hydroxo-bridged di-iron(III) products. The recent crystal structures of copper(II)- and iron(III)-bound frog M ferritin at 2.8 Å resolution [Bertini; et al. *J. Am. Chem. Soc.* **2012**, *134*, 6169−6176] provided an opportunity to theoretically investigate the detailed structures of the reactant state and products. In this study, the quantum mechanical/molecular mechanical ONIOM method is used to structurally optimize a series of single-subunit models with various hydration, protonation, and coordination states of the ferroxidase site. Calculated exchange coupling constants (J), Mössbauer parameters, and time-dependent density functional theoretical (TD-DFT) circular dichroism spectra with electronic embedding are compared with the available experimental data. The di-iron(II) model with the most experimentally consistent structural and spectroscopic parameters has 5-coordinate iron centers with Glu23, Glu58, His61, and two waters completing one coordination sphere, and His54, Glu58, Glu103, and Asp140 completing the other. In contrast to a previously proposed structure, Gln137 is not directly coordinated, but it is involved in hydrogen bonding with several iron ligands. For the di-iron(III) products, we find that a μ-oxo-bridged and two doubly bridged (μ-hydroxo and μ-oxo/hydroxo) species are likely coproduced. Although four quadrupole doublets were observed experimentally, we find that two doublets may arise from a single asymmetrically coordinated ferroxidase site. These proposed key structures will help to explore the pathway connecting the di-Fe(II) state to the peroxo intermediate and the branching mechanisms leading to the multiple products.

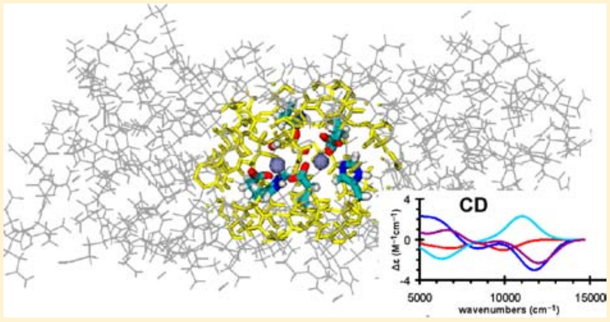

1. INTRODUCTION

Ferritins are ubiquitous iron storage proteins found in all forms of life that are critical for preventing toxic radical chemistry and oxidative damage.[1,2] The maxi-ferritins of animals, plants, and bacteria are composed of a 12 nm diameter protein shell surrounding an 8 nm cavity that can store up to 4500 iron atoms in the form of a hydrated iron oxide. The shell comprises 24 subunits, each structured as a 4-α-helix bundle. Animal ferritins have H and L subunits, which have different rates of iron uptake and mineralization, and occur in various ratios with tissue-specific distributions.[3] H subunits and a variant, M, have ferroxidase sites that catalyze an important early step in the biomineralization process:[4]

$$2Fe^{2+} + O_2 + H_2O \rightarrow [Fe(III){-}O{-}Fe(III)] + H_2O_2 \quad (1)$$

The next step for the di-Fe(III) products and the mechanism of Fe(II)-site renewal is not clear. One hypothesis is that the ferroxidase products migrate to a nearby site where they react with subsequently formed dimers to form multimers that eventually enter the cavity at the end of a 20 Å long channel. This was supported by (1) the broadening of ^{13}C NMR peaks of specific side chains in frog M ferritin (FrMF) subunits, attributed to the effect of nearby paramagnetic Fe(III) products,[5] (2) mutagenesis of residues along the channel, inhibiting normal function,[6] and (3) magnetic susceptibility indicating multimer formation. By contrast, it was recently shown that the Fe(III) transport protein transferrin can scavenge Fe(III) from human H (HuHF) and *P. furiosus* ferritin (PfFtn), and that it can only bind Fe(III) located at the ferroxidase sites, suggesting that the products had not migrated.[7] This conclusion was supported by isothermal calorimetry measurements showing that Fe(II) binding was partially impeded in an Fe(III)-containing ferritin. Furthermore, EPR detection of a mixed-valence species led to the conclusion that Fe(II) displaces Fe(III) sequentially. This seemingly contradictory behavior (i.e., Fe(III) product migration versus indefinite ferroxidase site occupation until displacement) may be due to differences in the time between additions of Fe(II). A previous study involving consecutive additions of 2Fe(II)/subunit to apo-HuHF indicated that full

Received: March 12, 2013
Revised: June 5, 2013
Accepted: July 6, 2013
Published: July 18, 2013

regeneration of Fe(II) oxidation activity requires more than 24 h.[8] The incubation times in the NMR and transferrin/ITC/EPR studies were 48 h and less than 12 h (20 min for the transferrin assay), respectively; thus, turnover had not yet been completed in the latter case. Both mechanisms of Fe(II) binding and Fe(III) migration may be operable and dependent on the rate of Fe(II) uptake.

The first iron-bound X-ray crystal structure of a higher eukaryotic ferritin (frog M) was recently obtained at 2.7 Å resolution, identifying the protein-derived ligands of Fe(III) as Glu23 and His61 at the A site and Glu103 at the B site,[9] as shown in Figure 1. The two centers are bridged by Glu58, and the Fe−Fe distance of 3.1 ± 0.1 Å, supported by a 3.00 Å distance from EXAFS analysis,[10] suggests the presence of an unresolved bridging μ-oxo/hydroxo ligand. A crystal structure of a Cu(II) analogue of the Fe(II)-bound state was also obtained, showing an increased metal−metal distance (4.3 ± 0.4 Å), and an additional ligand at the B site, His54, which was in conformation different from that in the Fe(III)-bound structure. Support for the suitability of the Cu(II) analogue came from a third structure, in which a demineralized ferritin crystal was soaked with Fe(II) under aerobic conditions for a short time (1 min). In the resulting structure, iron (likely ferric) occupied various positions in different subunits, aligning well with the ferroxidase sites of the Fe(III)-soaked crystal in some subunits, whereas in others, the longer Fe−Fe distances suggested that the iron was still in the initial Fe(II) positions. In the latter subunits, the ferroxidase sites overlaid well with the Cu(II)-bound sites, including the conformation of His54.

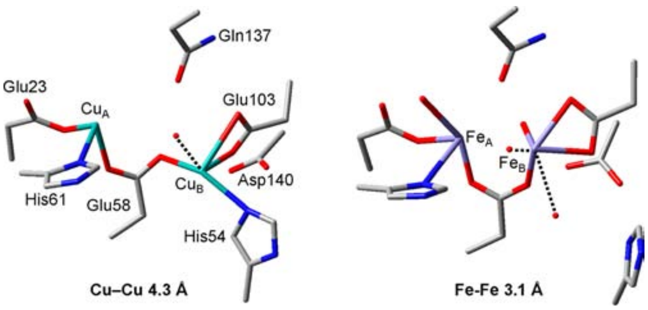

Figure 1. X-ray crystal structures of Cu(II)- (left) and Fe(III)-bound (right) frog M ferritin ferroxidase sites (PDB IDs: 3RE7 and 3RBC). M−M distances are given as averages over the 24 subunits.

Interestingly, Gln137 and Asp140 are not coordinated in the Cu(II) and Fe(III) derivatives, whereas they are bound to the B site in a 2.8 Å resolution FrMF crystal structure cocrystallized with Mg(II).[11] The analogous Gln residue in HuHF (Gln141) is also not coordinated in a 1.8 Å resolution Zn(II)-bound structure.[12] Gln137 (using the FrMF sequence) is a conserved residue in FrMF, HuHF, and PfFtn, along with the aforementioned Glu23, Glu58, His61, and Glu103, but Asp140 is a noncoordinating Ala in HuHF, and a Glu in PfFtn. The discrepancy in Gln137 and Asp140 positions in the crystal structures is important, because site-directed mutagenesis studies have demonstrated by monitoring the absorbance of a peroxo intermediate and products of the ferroxidase reaction that these residues are necessary for normal function. Specifically, when Asp140 in FrMF is substituted by Ala, as in HuHF, the Fe(II) binding affinity decreases.[13] If, instead, Asp140 is substituted by the more strongly coordinating His residue that is present in the catalytic sites of di-iron cofactor enzymes, such as methane monooxygenase, ribonucleotide reductase, and Δ^9 desaturase, the peroxo intermediate is not observed. The Gln137 position is occupied by Glu in the di-iron cofactor enzymes, which have two bridging Glu residues, and when this substitution is made in either FrMF or HuHF, the peroxo intermediate is not formed and the products have different absorbance spectra.[8,13]

A third Fe(II) binding site ~6 Å from the ferroxidase site (Fe−Fe) has been identified in a PfFtn crystal structure. Similar sites were also occupied by Tb(III) in HuHF,[14] Co(II) in FrMF,[15] and Cu(II) in all but one subunit of FrMF, whereas it was unoccupied in several other structures, including HuHF with Zn(II) and FrMF with Mg(II) or Fe(III). Isothermal calorimetry and absorption data indicate three Fe(II) binding events in PfFtn and HuHF under anaerobic conditions.[7] As two Glu residues (57 and 136) of the third site are conserved in PfFtn, HuHF, and FrMF, one may surmise that Fe(II) binds to the third site in each and that Cu(II) is a better analog for Fe(II) than Mg(II) or Zn(II). However, a circular dichroism (CD) and magnetic CD (MCD) study of FrMF showed that only two Fe(II)'s bind, as the band intensities did not increase after addition of Fe(II) beyond two per subunit.[16] Furthermore, a concerted and cooperative binding process was indicated by the identical, sigmoidal binding curves for each CD transition. The apparent differences in Fe(II) binding between FrMF and other species may be attributed to the nonconserved residues, including Asp140 and His54. To justify the choice of the Cu(II)-bound FrMF over the higher resolution (1.4 Å) Co(II)-bound structure, we note that in addition to the two Co(II)'s at the ferroxidase site and one at the third site, a fourth nearby position is occupied. As our aim is to model FrMF with only two Fe(II)'s present, the extraneous Co(II) would be removed, but the residues to which they were bound would still be in non-native conformations. Most significantly, Asp140 and His54 are bound to these Co(II)'s and are not in the vicinity of the ferroxidase site. On the other hand, the Cu(II)-bound ferritin is not complicated by a fourth site, and one of the subunits has a free third site, making it an ideal structure on which to base our di-Fe(II) models.

The moderate resolution, partial occupancy of ferroxidase sites,[9] and use of Fe(II) analogues in ferritin crystal structures precludes a detailed description of the positions, binding modes, and protonation states of protein- and water-derived ligands by crystallography alone; complementary spectroscopic and theoretical studies are necessary to define the structures of the Fe(II), Fe(III), and intermediate states. In the case of Fe(II), the CD/MCD analysis indicated two weakly antiferromagnetically coupled ($J = -0.8$ cm^{-1}) 5-coordinate centers with an $M_s = \pm 2$ ground state.[16] Such weak coupling is consistent with a μ-1,3 bridging Glu but not with water-derived bridging ligands. A peroxo intermediate with a very short, 2.53 Å Fe−Fe distance has been characterized by stopped-flow absorption,[17] EXAFS,[10] resonance Raman,[18] and Mössbauer[19−21] spectroscopies. Decay of the peroxo intermediate to Fe(III) products has been monitored by rapid-freeze-quench Mössbauer spectroscopy using FrMF and HuHF.[19,20] Although the spectra of HuHF were consistent with a single type of dimer product, parallel formation of multiple diamagnetic species (i.e., antiferromagnetically coupled Fe(III) dimers) and paramagnetic polynuclear clusters was observed for FrMF. Notably, in a previous Mössbauer study of HuHF using longer reaction times (0.5−30 min versus 50 ms−10 min), two separate dimers were detected, followed by monomers, and then small clusters,[22] which is the expected order if Fe(III) is sequentially displaced by Fe(II).[7]

Previous density functional theoretical (DFT) studies have examined the hydration of the ferroxidase center of FrMF,[23] the structures of the Zn(II)- and Fe(II)-bound HuHF,[24,25] and simple models of the peroxo intermediate.[26] The optimized geometry of a μ-hydroxo-bridged Zn(II) model was most consistent with the HuHF crystal structure,[24] and substitution with Fe(II) resulted in little change.[25] Spectroscopic information regarding the Fe(II)-bound HuHF is limited, but the CD/MCD analysis did not indicate a μ-hydroxo bridge in FrMF.[16] In the DFT study of FrMF, the two Fe(II) binding sites of the ferroxidase center were modeled separately with various numbers of aqua ligands, and the optimized structures were evaluated on the basis of energetic criteria.[23] Sites A and B were found to favor 5- and 4-coordinate geometries, respectively, which is inconsistent with the CD/MCD data, but the small models were based on the Mg(II)-derivative of FrMF with the amino acid backbones fixed in their crystallographic positions. Other related theoretical studies include molecular dynamics simulation of Fe(II) entry and binding to apo-HuHF,[27] flavin docking and electron transfer through ferritins,[28] O_2 entry into HuHF,[29] and our recent quantum mechanical/molecular mechanical (QM/MM) investigation of polymerization of phenylacetylene by a rhodium complex encapsulated in apoferritin.[30]

Here, we present a QM/MM analysis of the Fe(II)-bound ferroxidase center and di-Fe(III) products of FrMF, basing our models on the recent Cu(II)- and Fe(III)-loaded crystal structures. The Cu(II) derivative provides the best representation of the Fe(II)-bound structure to date, and it has unique features (e.g., His54 ligation) that were not present in previous models. In the Fe(III)-loaded structure, the inability to resolve the bridging ligands warrants a theoretical investigation.

In contrast to small QM-only models, the QM/MM method with a large system allows for structural flexibility while imposing more realistic constraints on the conformations of the ferroxidase site residues, which is crucial given the uncertainty of the initial atomic positions. Time-dependent DFT (TD-DFT)-derived CD spectra provide an important point of comparison between experiments and our series of Fe(II)-state models with various water-derived ligands and coordination states of Glu, Gln, and Asp residues. Because there was no indication of a third Fe(II) binding site in the CD/MCD study,[16] we include only two Fe(II) sites in the models. For our singly or doubly μ-oxo/hydroxo-bridged di-Fe(III) product models, the best links to experiment are the optimized Fe−Fe distances and calculated Mössbauer parameters. By correlating the calculated structural and spectroscopic properties with experiment, we identify the most likely structure of the reactant state and propose several products. This is a necessary first step before the ferroxidase reaction pathway and mechanism can be theoretically explored.

2. COMPUTATIONAL DETAILS

2.1. System Preparation. The computational models in this work represent single subunits from the Cu(II)- and Fe(III)-bound FrMF crystal structures[9] (PDB IDs: 3RE7 and 3RBC). Specifically, subunits K and C were selected for the Cu(II) and Fe(III) structures, respectively, on the basis of analyses presented in the Results and Discussion. All metal ions except the two bound in each ferroxidase site were removed. These were present mostly at interfaces between subunits, and while those at the 3-fold axis may indicate binding positions in an entry pore,[15] others may not be physiologically relevant. The Cu(II) centers were replaced with Fe(II). Hydrogen atoms were added using the psfgen plug-in of VMD.[31] Histidine protonation states were assigned by visual inspection of their local environment. His54 was protonated at N_δ when bound to Fe(II), and N_ε when in the alternate conformation of the Fe(III)-containing subunit. In both subunit models, His45 and 169 were protonated at N_δ, whereas His9, 56, 61, 114, and 124 were protonated at N_ε. The overall charges were −4 and −2 for the Fe(II)- and Fe(III)-bound subunits, respectively, before adding any bridging μ-oxo/hydroxo groups. The total number of atoms was ~2950, varying with the bridging groups and number of waters included.

The initial structures of the two subunits were relaxed through a series of MM minimizations, using an Amber force field[32] and NAMD.[33] The hydrogen positions were optimized first, followed by the water molecules, and finally, all MM atoms within 9 Å of either iron center, selected on a per-atom basis. Atoms beyond 9 Å were not optimized to avoid major reorganization of the subunit surface because of the lack of neighboring subunits and a solvent pool. The Glu57 and Glu136 C_δ atoms were also fixed to their crystallographic positions because of large conformational changes during initial optimizations.

If it were allowed to fully relax, a single subunit of ferritin would not function normally and would have a significantly different conformation than in the 24-subunit, assembled form. Indeed, dimers (or trimers) of human H chains oxidize Fe(II) at about 10% of the rate of assembled HuHF.[34] The cooperativity of Fe(II) binding (Hill coefficient $n = 3$), noted above, was observed under anaerobic conditions, demonstrating the important role of intersubunit protein−protein interactions.[16] Furthermore, the thermal melting point of a HuHF mutant with fewer intersubunit hydrogen bonds is still more than 30 °C higher than that of the subunit monomer.[35] However, single subunit computational models can be sufficient for the present analysis of the ferroxidase site that does not involve dynamic binding or dissociation processes. A key point is that the model is based on the X-ray structure of assembled ferritin, and only atoms within 9 Å (<15% of the atoms in the subunit model) of the ferroxidase site are allowed to relax; thus, the functionally relevant conformation is maintained, and the surface residues are frozen in the position they had adopted in the assembled cluster. Conformational changes that occur during the binding and oxidation processes are taken into account, as the models are based on two separate crystals, one with the Fe(II) analogue Cu(II) bound, and one with Fe(III) bound.

2.2. ONIOM Method. QM/MM calculations were performed using the two-layer ONIOM method,[36−39] in which the ONIOM energy is extrapolated as follows:

$$E(\text{ONIOM}) = E(\text{real, MM}) + E(\text{model, QM}) - E(\text{model, MM}) \quad (2)$$

The "real" system includes all atoms and is only calculated at the efficient MM level. The "model" system is an inner layer including the active site that is used in both QM and MM calculations. Bonds between the two regions are capped by hydrogen link atoms for the model calculations. Cross-region electrostatic interactions can be treated classically using the mechanical embedding (ME) scheme, or the MM charges can be included in the QM Hamiltonian in the electronic embedding (EE) scheme.

In this study, the hybrid density functional, B3LYP,[40−42] and the Amber force field[32] were used for the QM and MM methods, respectively. This combination has been effectively used to investigate di-iron sites in methane monooxygenase[43] and *myo*-inositol oxygenase.[44] The broken symmetry formalism[45] was used to approximate the antiferromagnetically coupled state of the di-Fe(III) site, whereas the weakly coupled di-Fe(II) system was modeled in a high spin ($S = 4$) state. The SDD effective core potential basis set[46,47] was used for iron, and 6-31G(d)[48−51] was used for the other atoms for geometry optimizations. The adequacy of this basis set was verified using def-TZVP-optimized structures of selected models as references.[52] The Amber hydroxyl group and heme-iron nonbonded van der Waals parameters were used for hydroxo/oxo ligands and iron centers, respectively. This is not ideal, but the effects should be negligible

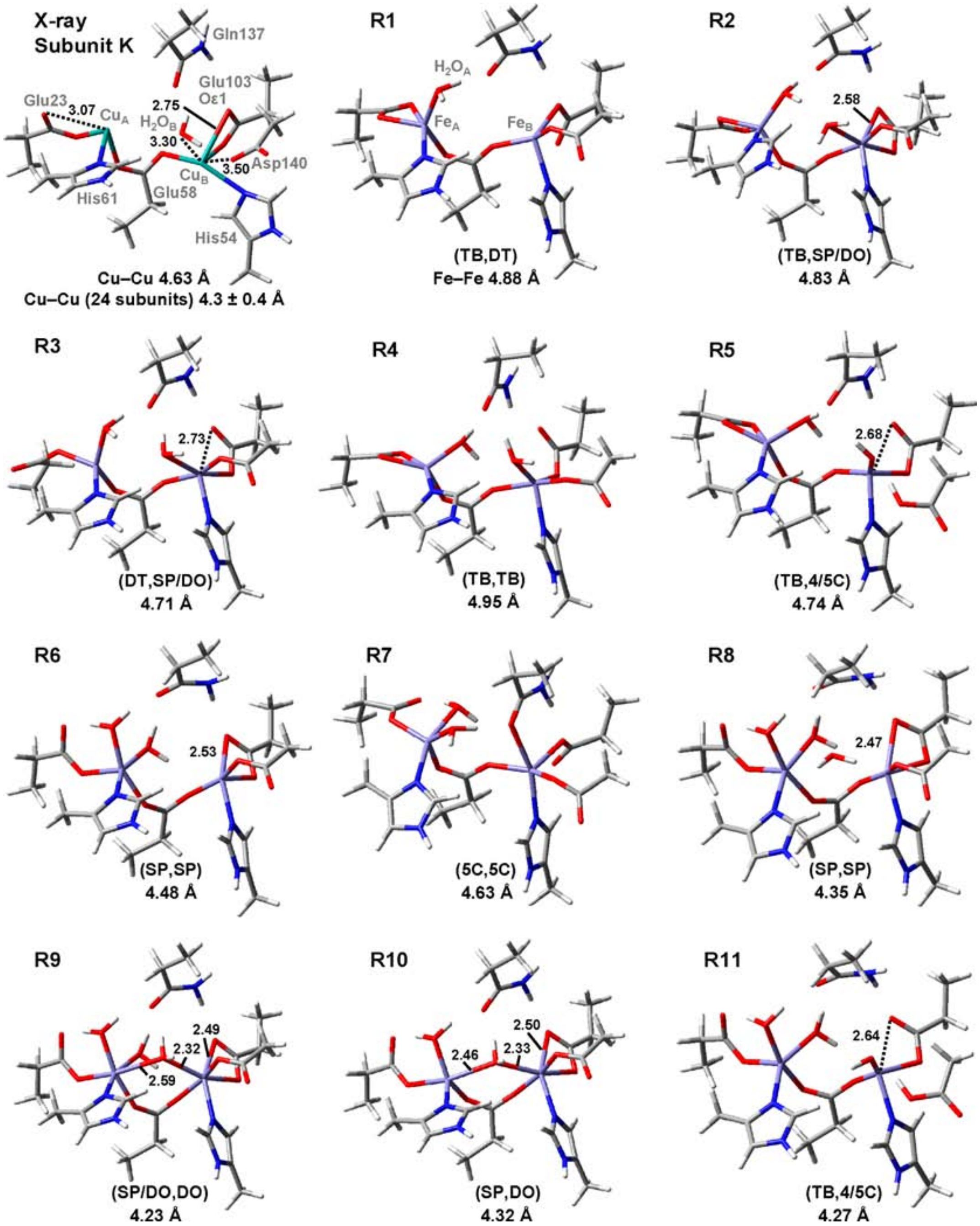

Figure 2. QM/MM-optimized di-Fe(II) models and initial crystallographic structure, including metal−metal distances. Only the QM layer is shown. Ligand field geometries are given for (Fe_A, Fe_B) as follows: TB, trigonal bipyramidal; SP, square pyramidal; DO, distorted octahedral; DT, distorted tetrahedral; 4/5C, 4- or 5-coordinate.

because these atoms are far from the QM/MM boundary (see below). The bonded parameters for these model-system groups do not need to be accurate, as their MM energy and gradient terms cancel in the ONIOM expression. Atomic charges for the model region were derived from Merz−Singh−Kollman[53,54] electrostatic potential (MK-ESP) analyses of geometry-optimized small models consisting of the same atoms as the QM layer, plus the hydrogen link atoms. These charges were maintained throughout the optimizations following the ONIOM-ME scheme. Atoms beyond 9 Å from either iron and the Glu57 and Glu136 C_δ atoms were fixed to their crystallographic positions, as in the MM minimizations. Local minima were verified by ONIOM harmonic frequency analysis taking into account all 389−411 (depending on the specific model) flexible atoms. All ONIOM and QM-only calculations were performed with Gaussian 09.[55] The ONIOM workflow was assisted by the TAO toolkit.[56]

The QM layer included the side chains of Glu23, Glu58, His61, Glu103, Gln137, Asp140, and, in the Fe(II)-containing models, His54. The C_β−C_α bond was the QM/MM boundary for each of these residues. Water molecules present in the crystal structure near the ferroxidase site were included in the QM layer, as were additional water-derived ligands in the various models described below. The charge of the QM layer was neutral in the Fe(II) models and −1 to +1 in the Fe(III) models, depending on the composition of the bridging ligands. The QM layers ranged from 73 to 84 atoms, including link hydrogens.

2.3. Spectroscopic Calculations. CD transitions were calculated for ONIOM-ME-optimized models using TD-DFT at the B3LYP/

def2-TZVP[57] level. The use of a smaller basis set, def-TZVP,[58,59] was also evaluated. Point charges representing the protein environment were included via ONIOM-EE. The CD spectra were generated by convoluting Gaussian functions with 0.3 eV widths at $1/e$ peak height using the Gaussian program.[60] The nature of each transition was determined by natural transition orbital (NTO)[61] and Mulliken analyses.

Mössbauer isomer shifts (δ) were calculated using their linear relationship with the electron density at each iron nucleus ($\rho(0)$):

$$\delta = \alpha\rho(0) + C \tag{3}$$

where α and C are constants that are specific to the employed level of theory (i.e., functional and basis set). Single-point calculations for QM-only models with ONIOM-ME-optimized geometries were carried out with the B3LYP functional, the Wachters[62] basis set without f functions for iron, and cc-pVDZ[63] for other atoms. Values for $\rho(0)$ were then obtained using AIMAll.[64] The α and C constants were −0.347 271 and +4033.261 027, respectively, as derived by Bochevarov et al.,[65] who applied the same functional and basis set to a training set consisting of Fe(III) and Fe(IV) compounds. The average error for the training set compounds was 0.03 mm/s using crystallographic structures, but for optimized protein-bound structures, errors may be on the order of 0.1 mm/s.[65]

Mössbauer quadrupole splittings (ΔE_Q) were determined from the electric field gradient (EFG) at each iron nucleus, according to

$$\Delta E_Q = \frac{1}{2}eQV_{zz}\sqrt{1 + \frac{\eta^2}{3}} \tag{4}$$

where e is the elementary charge, Q is the nuclear quadrupole moment of ^{57}Fe (0.16 barn),[66] and η is the asymmetry parameter, $(|V_{xx} - V_{yy}|/V_{zz}|$, in a coordinate system where the EFG tensors (V) have the order $V_{zz} \geq V_{xx} \geq V_{yy}$. The ONIOM-EE method was used to calculate the EFG tensors with the same functionals, basis sets, and geometries as for the isomer shifts. Errors are estimated to be <0.3 mm/s.[65]

Heisenberg exchange coupling constants, J, of the spin-Hamiltonian

$$H = -2JS_AS_B \tag{5}$$

were evaluated through pairs of broken symmetry (BS) and high spin (HS) calculations, according to Yamaguchi's expression[67]

$$J = -\frac{E_{HS} - E_{BS}}{\langle S_{HS}{}^2\rangle - \langle S_{BS}{}^2\rangle} \tag{6}$$

These energies and $\langle S^2\rangle$ values were obtained from single-point calculations at the optimized geometries, using the same level of theory (B3LYP/SDD (Fe),6-31G(d) (others)). The effects of electronic embedding and larger basis sets were tested and found to be insignificant. Functional dependence is more pronounced, but hybrids such as B3LYP are preferred over pure functionals that tend to overestimate J values.[68]

3. RESULTS AND DISCUSSION

3.1. Structural Models of the Di-Fe(II) Site. The computational models of the di-Fe(II) site were based on a 2.8 Å resolution X-ray crystal structure of Cu(II)-bound frog M ferritin, refined with 24 independent subunits.[9] There is considerable variation in the atomic positions among the subunits, as indicated by the 0.4 Å estimated standard deviation (esd) of the differences in Cu−Cu distances. To find an approximately average ferroxidase site, the root-mean-square-deviation (rmsd) of several critical distances (Cu_A−Glu23(Oε1), −Glu23(Oε2), −Glu58(Oε1), −His61(Nδ); Cu_B−Glu58(Oε2), −His54(Nε), −Glu103(Oε1), −Glu103(Oε2); and Cu_A−Cu_B) relative to their respective averages was calculated for each subunit. Subunit K was found to have a low rmsd (0.15 Å), and the absence of copper bound in the third site near the ferroxidase center made it the clear choice to serve as the basis for the computational models. The Cu_A−Cu_B distance in subunit K, and thus our initial Fe_A−Fe_B distance, is 4.63 Å, which happens to be long relative to the average distance of 4.3 ± 0.4 Å.

3.1.1. Coordination Environments. In subunit K, there is one water resolved at the B site and none at the A site. If Glu23 and Glu103 are coordinated in monodentate and bidentate modes, respectively, the B site is 5-coordinate, whereas the A site is 4-coordinate, which is inconsistent with the trigonal bipyramidal and square pyramidal assignments derived from MCD data. However, at 2.8 Å resolution, the number and location of waters is highly uncertain. Considering the exposure of the ferroxidase site to the solvent-filled inner cavity, it is very likely that there are more aqua ligands; thus, we examined models with one or two waters added to the A site (H_2O_A), as well as models with and without the B-site water (H_2O_B). The 11 optimized models, shown in Figure 2, are further distinguished by the variable coordination mode of Glu23 and Glu103, the coordination, or lack thereof, of Asp140, and the various hydrogen bonds involving waters. We did not investigate μ-hydroxo-bridged models because the di-Fe(II) system is known to be very weakly coupled, as described in Section 3.1.3.

Among the models with one H_2O_A (**R1**−**R5**), **R1** is the only model lacking a H_2O/OH^- ligand at the B site. Consequently, the coordination environment of Fe_B is 4-coordinate and thus inconsistent with experiment. Models **R2**−**R5** that are optimized with inclusion of H_2O_B initially in its crystallographic position have 4−6-coordinate Fe_B. As indicated in Figure 2, the specific assignments for the coordination geometry of Fe_B are not always clear. For example, **R5**, which lacks Asp40 coordination due to proton transfer from H_2O_B, has a 4−5-coordinate Fe_B depending on whether the 2.68 Å Fe_B−Glu103(Oε1) interaction is considered to be a bond.

Structures **R6**−**11** have an additional aqua ligand bound either terminally to Fe_A or in a bridging mode. Interestingly, one structure (**R7**) was found with Gln137 coordinated to Fe_B (2.43 Å). Gln137 is required for formation of the peroxo intermediate and has been considered a ligand of Fe_B;[13] however, in the Cu-bound crystal structure, the average Gln(Oε1)−Cu_A/Cu_B distances are 3.49/3.81 Å (3.76/3.81 Å in subunit K). In all models but **R7**, the Gln(Oε1)−Fe_B bond is prevented either by the presence of H_2O_B or by a hydrogen bond with an H_2O_A, coupled with the long initial distance from Fe_B. **R7** has experimentally consistent 5-coordinate sites (the specific ligand-field geometries are not clear) and should not be eliminated from consideration despite the large deviation from the crystal structure. In contrast to **R6** and **R7**, models **R8**−**R11** were optimized with an initial H_2O_B. In **R8**, H_2O_B is no longer bound to Fe_B but forms a hydrogen bond with Asp140, resulting in a structure similar to **R6**. Alternatively, H_2O_B can occupy the weakly bridging position found in **R9**, with μ-H_2O_B−Fe_A/Fe_B distances of 2.59/2.32 Å, in which case Fe_A is 5−6-coordinate and Fe_B is approximately octahedral. If one H_2O_A is removed from **R9**, the bridging interaction is strengthened, as indicated by the shortened μ-H_2O_B−Fe_A distance (2.46 Å) in **R10**, in which case the geometry at Fe_A becomes square pyramidal, but Fe_B remains approximately octahedral. As with the $1H_2O_A$ models (**R1**−**R5**), a structure, **R11**, can be found with the loss of Asp140 coordination, reducing the coordination number to 4 or 5, depending again on the assignment of the 2.64 Å Fe_B−Glu103(Oε1) interaction.

Overall, no single model can be definitively described as having one square pyramidal and one trigonal bipyramidal site. The distorted geometries and, in some cases, weak metal—ligand interactions present difficulties in assigning the environments. However, models **R4** and **R6**—**R8** clearly have two 5-coordinate iron centers and are thus good candidates for the Fe(II)-bound state. Further structural analysis and calculated spectral parameters are required to identify the best model.

3.1.2. Fe—Fe Distances and the Coordination Mode of Glu23. An important difference between models with one water bound to Fe_A (**R1**—**R5**) and those with two or more (**R6**—**R11**) is the coordination mode of Glu23. With the exception of **R3**, the former group has bidentate Glu23, whereas the latter has monodentate *syn* coordination and a hydrogen bond to an H_2O_A. **R3** is the one model with monodentate *anti* coordination of Glu23. This difference between the two groups contributes to the longer Fe—Fe distances (4.71—4.95 Å) in **R1**—**R5** than **R6**—**R11** (4.23—4.63 Å) (see Figure 2). The second H_2O_A of **R6**—**R11** prevents bidentate coordination of Glu23 and forms hydrogen bonds with Gln137 and the bridging Glu58, leading to migration of Fe_A toward Fe_B. The effect of this hydrogen network on the Fe—Fe distance is demonstrated by model **R7**, in which it is disrupted by rotation of the Glu23 carboxylate group and coordination of Gln137 to Fe_B, resulting in the only Fe—Fe distance in the **R6**—**R11** group over 4.5 Å (4.63 Å, specifically). Models **R4** and **R5** also have these hydrogen bonds, but the bidentate Glu23 restricts Fe_A migration.

The shorter distances of the **R6**—**R11** group are well within the experimental error range, 4.3 ± 0.4 Å, whereas those of **R1**—**R5** are too long. The favored structures, in terms of coordination geometry, **R4** and **R6**—**R8** have Fe—Fe distance of 4.95, 4.48, 4.63, and 4.35 Å, respectively; thus, **R6**—**R8** are most consistent with the crystal structure. However, direct comparisons of optimized structural parameters with those of the crystal structure have limited value due to both the 2.8 Å resolution and the substitution of Fe for the cocrystallized Cu. Comparisons of M—L bond lengths, in particular, are not justified because of the long distances in the crystal structure that were attributed to partial occupancy of the ferroxidase sites.[9]

3.1.3. Heisenberg Exchange Coupling Constants. The exchange coupling constant, *J*, for the Fe(II)-bound state has been determined through analysis of VTVH MCD data to be approximately $-0.8\ cm^{-1}$,[16] indicating very weak antiferromagnetic coupling. This is consistent with a μ-1,3 carboxylate bridge and the absence of water-derived ligands, as previous examples of μ-aqua-bridged Fe(II) dimers have been ferromagnetically coupled[69,70] and μ-hydroxo bridges promote stronger antiferromagnetic coupling ($J \approx -14\ cm^{-1}$).[71] The calculated *J* values (Supporting Information Table S1) for **R1**—**R9** and **R11** lie in a small range (-0.2 to $-1.4\ cm^{-1}$) and can all be considered consistent with experiment. The *J* values of the μ-aqua-bridged models, **R9** ($-0.9\ cm^{-1}$) and **R10** ($-2.6\ cm^{-1}$) do not indicate the expected ferromagnetic coupling for such systems. This is likely due to the weak nature of the bridging interactions, characterized by μ-H_2O—Fe bond distances of 2.46 and 2.33 Å in **R10** (2.59 and 2.32 Å in **R9**), versus 2.19 and 2.17 Å in a di-Fe(II) model compound.[70] The significant deviation of the **R10** *J*-value from the other models and from the experiment disfavor it as a structural candidate for the Fe(II)-bound state.

3.1.4. TD-DFT Simulation of CD Spectra. The CD/MCD spectra of the Fe(II)-bound state, taken at 1.7 K, show features at 5025, 7600, 9900, and 11 150 cm^{-1} (see CD spectrum in Figure 3), attributed to two d—d transitions at each iron center.[16] These correspond to $(t_{2g})^4(e_g)^2 \rightarrow (t_{2g})^3(e_g)^3$ single-electron excitations, using an octahedral field as an example. Lower symmetry environments give rise to distinct splitting patterns of the degenerate orbitals. Absorption data for mononuclear nonheme Fe(II)-model complexes show ligand-dependent variations in d—d transition energies, but in general, those with trigonal bipyramidal geometries have transitions at ~5000 and ~9000 cm^{-1}, whereas the higher energy transition is >10 000 cm^{-1} in square pyramidal models.[72] Tetrahedral and octahedral complexes have two transitions at ~5000 and ~10 000 cm^{-1}, respectively, reflecting the different ligand field strengths. This model complex data, together with zero-field splitting values (*D*) determined through analysis of VTVH MCD data of the Fe(II)-bound ferritin, allowed the transitions at 7600 and 11 150 cm^{-1} to be assigned to a single iron center with square pyramidal geometry, whereas those at 5025 and 9900 cm^{-1} were assigned to a second, trigonal-bipyramidally coordinated iron.[16]

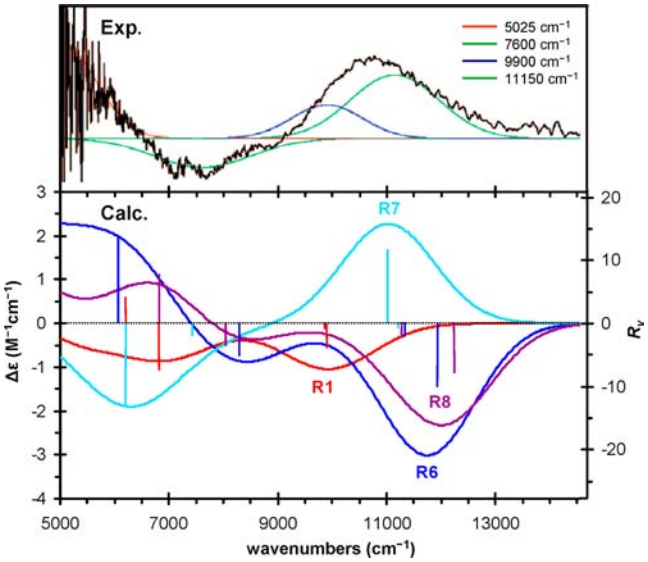

Figure 3. Calculated CD spectra for four di-Fe(II) models compared with the 1.7 K experimental spectrum and deconvolution.[16] The right axis (rotatory strength) corresponds to the line spectra. The top portion of this figure is modified and reprinted with permission from ref 16. Copyright 2008 American Chemical Society.

CD transition energies and rotatory strengths were calculated for each model complex using TD-DFT with B3LYP/def2-TZVP and ONIOM-EE to capture electrostatic perturbations due to the protein environment. This strategy recently proved useful for identifying the structure of the peroxo intermediate of the di-iron nonheme enzyme, Δ^9 desaturase.[73] Basis set and electronic embedding effects were evaluated using **R6** as a test system. The velocity and length gauge formulations of rotatory strength (R_v, R_l) are expected to converge with higher quality basis sets, and indeed, Table 1 shows that the difference between the two values is significantly reduced for several roots with def2-TZVP compared with def-TZVP. For example, the rotatory strengths of root 5 without electronic embedding are 22.7/7.3 (R_v/R_l; 10^{-40} cgs units) with def-TZVP, and 13.8/11.8

Table 1. Calculated CD Transitions for Model R6 with Two Basis Sets and with and without Electronic Embedding

	QM Only					
	def-TZVP			def2-TZVP		
root	$\tilde{\nu}$ (cm^{-1})	R_v[a]	R_l[a]	$\tilde{\nu}$ (cm^{-1})	R_v[a]	R_l[a]
1	1 891	−0.6	−9.0	2 468	−4.8	−10.2
2	2 604	−20.0	7.2	3 134	−0.4	5.3
3	3 812	20.7	12.4	4 286	13.3	11.5
4	3 961	6.7	13.9	4 482	6.9	8.7
5	5 489	22.7	7.3	5 923	11.4	8.2
6	7 894	−9.6	2.2	8 319	−6.3	−1.6
7	10 804	−10.5	−9.9	11 343	−6.4	−4.8
8	10 882	0.8	2.9	11 362	−6.3	−6.3
9	26 303	−0.5	2.4	26 524	−0.4	0.3
10	28 008	0.4	0.9	28 193	−0.7	−1.3
	ONIOM-EE					
	def-TZVP			def2-TZVP		
root	$\tilde{\nu}$ (cm^{-1})	R_v[a]	R_l[a]	$\tilde{\nu}$ (cm^{-1})	R_v[a]	R_l[a]
1	1 646	0.5	0.7	2 274	−4.7	−1.5
2	2 807	−25.8	4.0	3 322	−1.3	0.8
3	3 600	6.3	−7.6	4 109	1.4	−3.1
4	3 976	18.7	23.5	4 446	19.6	18.3
5	5 605	26.8	13.6	6 063	13.8	11.8
6	7 884	−9.0	5.9	8 316	−5.5	0.2
7	10 909	−0.3	2.3	11 354	−2.8	−1.2
8	11 274	−9.2	−7.2	11 821	−10.2	−9.5
9	20 444	2.4	14.1	20 774	2.3	2.1
10	22 778	0.7	4.9	22 964	−0.2	−0.3

[a] Rotatory strength in velocity (R_v) and length (R_l); representation in 10^{-40} cgs units (erg esu cm G^{-1}).

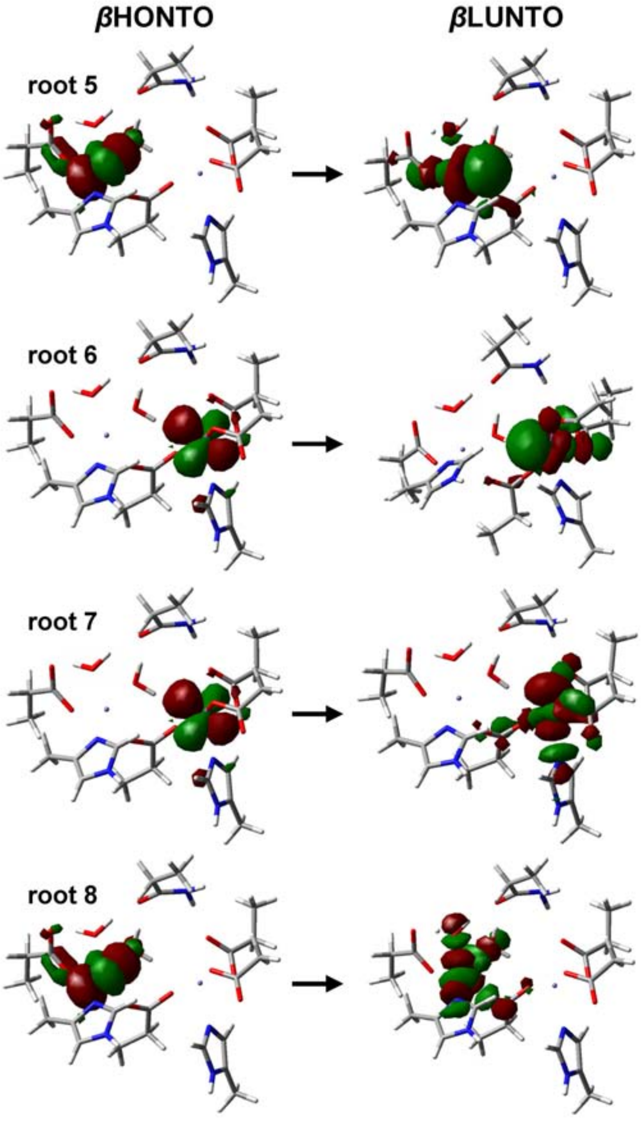

Figure 4. Highest occupied and lowest unoccupied β natural transition orbitals (βHONTO/βLUNTO) representing the dominant contributions (>90%) to the four CD transitions of model **R6** (Figure 3 and Table 2).

with def2-TZVP. The energies are ~500 cm^{-1} higher for each of the first eight roots with def2-TZVP. The protein environment can significantly affect relative transition intensities, as demonstrated by roots 7 and 8, which have R_v values of −6.4/−6.3 with EE and −2.8/−10.2 without EE. Energetic perturbations due to the protein environment range from −200 to +500 cm^{-1}, varying across the first eight roots. Overall, rotatory strengths are more sensitive to basis set and EE effects than are the excited-state energies, and at this level, even the signs can be incorrect. Hence, more weight is given to the calculated energies than the rotatory strengths when evaluating the models.

For each model, the lowest eight roots correspond to the eight single-electron, spin-allowed, d−d excitations that are expected for two high-spin d^6 centers. Among these, the four highest energy transitions (roots 5−8) are expected to correspond to the experimental peaks. To enable detailed comparison of these with the experiment and for correlation with the coordination environments, it is important to assign the transitions to specific iron centers. The ground-state Kohn−Sham orbitals involved in the most dominant transitions for each root did not always allow specific assignment because some d orbitals were highly delocalized between the two iron centers (Supporting Information Figure S1). However, natural transition orbital (NTO) analysis for model **R6** revealed localized excitations, as shown in Figure 4. For each root, the NTO eigenvalues were ~2 for the highest occupied and lowest occupied NTOs (HONTO/LUNTO), and <0.1 for the HONTO−1/LUNTO+1, indicating that each transition is dominated by a single particle/hole pair. As expected for a system with two square pyramidal sites, the four highest energy transitions are d$_\pi$ → d$_{x^2-y^2}$ (roots 7 and 8) and d$_\pi$ → d$_{z^2}$ (roots 5 and 6). An alternative method to assign the transitions is to compare the Fe(3d) Mulliken populations derived from the densities of the ground and each excited state. This method yields assignments consistent with those from the NTO analysis and was used for all models.

The calculated CD transition energies and assignments to specific iron centers for all models are presented in Table 2. The models that have four energetically ordered transitions alternating between iron centers, as in the experiment, are **R1**, **R3**, **R5**, and **R7**. However, the other models should not be removed from consideration because the two highest energy transitions (root 7 and root 8) are within 1000 cm^{-1} for most models (only 19 cm^{-1} for **R1**), and small structural distortions could affect the order. The transitions assigned to each iron center correlate well with the coordination environment in most cases. The distorted octahedral Fe$_B$ sites of **R9** and **R10** each have two CD transitions within 1000 cm^{-1} of 10 000

Table 2. Calculated CD Transitions and Assignments for All Di-Fe(II) Models and Comparison with Experiment

	$\tilde{\nu}$ (cm^{-1})									
model	root 5	root 6	root 7	root 8	Fe$_A$-based roots	Fe$_B$-based roots	deviation in Fe$_A$ splitting (exp1)[a]	deviation in Fe$_B$ splitting (exp1)[a]	deviation in Fe$_A$ splitting (exp2)[a]	deviation in Fe$_B$ splitting (exp2)[a]
R1	6200	6814	9 898	9 917	6,8	5,7	−448	−1177	−1773	148
R2	7204	8646	9 433	10 109	5,6	7,8	−2108	−4199	−3433	−2874
R3	6406	8874	9 338	10 224	5,7	6,8	−617	−3525	−1942	−2200
R4	6724	6837	9 532	9 777	6,7	5,8	−855	−1822	−2180	−497
R5	7019	7888	9 342	10 270	5,7	6,8	−1226	−2493	−2551	−1168
R6	6063	8316	11 354	11 821	5,8	6,7	2208	−1836	883	−511
R7	6237	7428	11 043	11 247	5,7	6,8	1256	−1057	−69	268
R8	6797	8051	11 292	12 121	5,8	6,7	1774	−1635	449	−310
R9	8020	9036	9 961	12 203	5,8	6,7	632	−3950	−693	−2625
R10	7684	9244	9 422	10 181	5,6	7,8	−1990	−4116	−3315	−2791
R11	5467,[b] 5778	7249	10 431	12 352	4,8	5,6,7	3335	c	2010	c
exp1	5025	7600	9 900	11 150	6,8	5,7				
exp2					5,7	6,8				

[a] Splitting refers to the difference in energy of the Fe$_A$- or Fe$_B$-based roots. Exp1 and exp2 indicate the transition assignments used for the experimental[16] reference splittings. [b] This root 4 energy is shown because roots 5−7 were all Fe$_B$-based. [c] No splitting is given because three Fe$_B$-based roots lie within the experimental energy region.

cm^{-1}, as expected. The trigonal bipyramidal sites (**R1** Fe$_A$, **R2** Fe$_A$, **R4** Fe$_{A/B}$, **R5** Fe$_A$), except **R11** Fe$_A$,[74] and the square pyramidal sites (**R6** Fe$_{A/B}$, **R8** Fe$_{A/B}$, **R9** Fe$_A$) have the expected larger splittings (1442−5758 cm^{-1}), and the high-energy transitions are below 10 000 cm^{-1} for the former, above for the latter. With this level of accuracy, the CD calculations may be able to aid in assigning more ambiguous sites. For example, the Fe$_B$ site of **R2** is described as square pyramidal if the weak, 2.58 Å interaction with Glu103(Oε1) is not considered to be a bond, but the 9433 and 10 109 cm^{-1} transitions suggest that a distorted octahedral assignment is more appropriate. On the other hand, the CD spectra for the distorted tetrahedral sites do not show the two low-energy transitions (∼5000 cm^{-1}) that are expected on the basis of the weaker ligand field. For these sites, the larger than expected splitting of, for example, **R3** Fe$_A$ (2933 cm^{-1}) can be attributed to the distorted geometry, whereas the high energies (6406 and 9338 cm^{-1}) may be due to systematic error of the TD-DFT calculation.

Rather than compare the calculated CD transition energies directly to experiment, the splitting between the two transitions at each iron site can be used, which reduces systematic error. Analysis of the experimental data indicated that the four localized CD transitions alternate between iron centers, giving splittings of 4875 (5025 and 9900 cm^{-1} transitions) and 3550 cm^{-1} (7600 and 11 150 cm^{-1} transitions), but specific assignment to Fe$_A$ and Fe$_B$ can only be inferred through inspection of the crystal structure. Thus, the calculated splittings must be compared to two sets of experimental reference data: 3550/4875 cm^{-1} for Fe$_A$/Fe$_B$ (exp1) or Fe$_B$/Fe$_A$ (exp2). Table 2 shows that with the exp1 reference, **R1** has the smallest deviations in splittings (−448/−1177 cm^{-1}), followed by **R7** (+1250/−1057 cm^{-1}). For **R1**, the larger deviation of −1177 cm^{-1} corresponds to the unlikely 4-coordinate Fe$_B$ site. The splittings of **R7** actually agree better with experiment when using the exp2 reference, as models **R6**−**R8** have deviations of +883/−511, −69/+268, and +449/−310 cm^{-1}, respectively, which are significantly smaller than those of the other models.

The low temperature (1.7 K) experimental CD spectrum and the calculated spectra of the four models with the most experimentally consistent splittings, **R1** and **R6**−**R8**, are plotted in Figure 3 (for CD spectra of the other models see Supporting Information Figure S2). The experimental spectrum has three major features: a strong, positive peak at ∼5025 cm^{-1}, a weak negative feature at ∼7600 cm^{-1}, and a strong positive feature at ∼10 500 cm^{-1} that was fit by weak and strong Gaussian band shapes at 9900 and 11 150 cm^{-1}, respectively. None of the calculated spectra have the correct signs for all three features, but this is not unexpected; incorrect signs were also obtained in the study of Δ^9 desaturase using the same computational method.[73] **R1** has two negative features of similar intensity, and it lacks a strong low-energy peak. The low- and intermediate-energy transitions are too close together (615 cm^{-1}) compared with the experimental difference of 2575 cm^{-1}, and the same is true for the two high-energy transitions, which are separated by 19 cm^{-1}, whereas the experimental difference is 1250 cm^{-1}. **R7** has a strong, positive feature at ∼11 000 cm^{-1} that agrees well with the experiment, but the intermediate-energy transition at 7428 cm^{-1} is too weak to be resolved, and the low-energy peak has the wrong sign. The gaps between the low- and intermediate-energy transitions (1192 cm^{-1}) and between the high-energy transitions (204 cm^{-1}) are improved relative to those of **R1**, but they are still too small. The spectra of **R6** and **R8** are similar to each other, as expected, because they differ mainly by the additional noncoordinated H_2O in **R8**, and they are more consistent with the experiment than the spectra of **R1** and **R7** in that there are three clearly resolved features. The low-energy, positive feature is present, as is the weaker, intermediate-energy negative peak, and the energy gap for **R6**, in particular (2253 cm^{-1}; 1254 cm^{-1} for **R8**), agrees well with the experimental gap. The strong, high-energy feature composed of two overlapping Gaussian band shapes is also present, and the energy differences of the two transitions in **R6** (467 cm^{-1}) and **R8** (829 cm^{-1}) are increased (i.e., improved) relative to those of **R1** and **R7**; however, the negative sign of this feature in both spectra is incorrect. Nevertheless, on the basis of the relative energies of all four transitions, the spectrum of **R6** agrees best with the experiment. It is clear simply from inspection of the spectra in Figure 3 that a constant shift of −1000 cm^{-1} would result in very good energetic agreement for **R6**. Indeed, each transition would be within 500 cm^{-1} of the

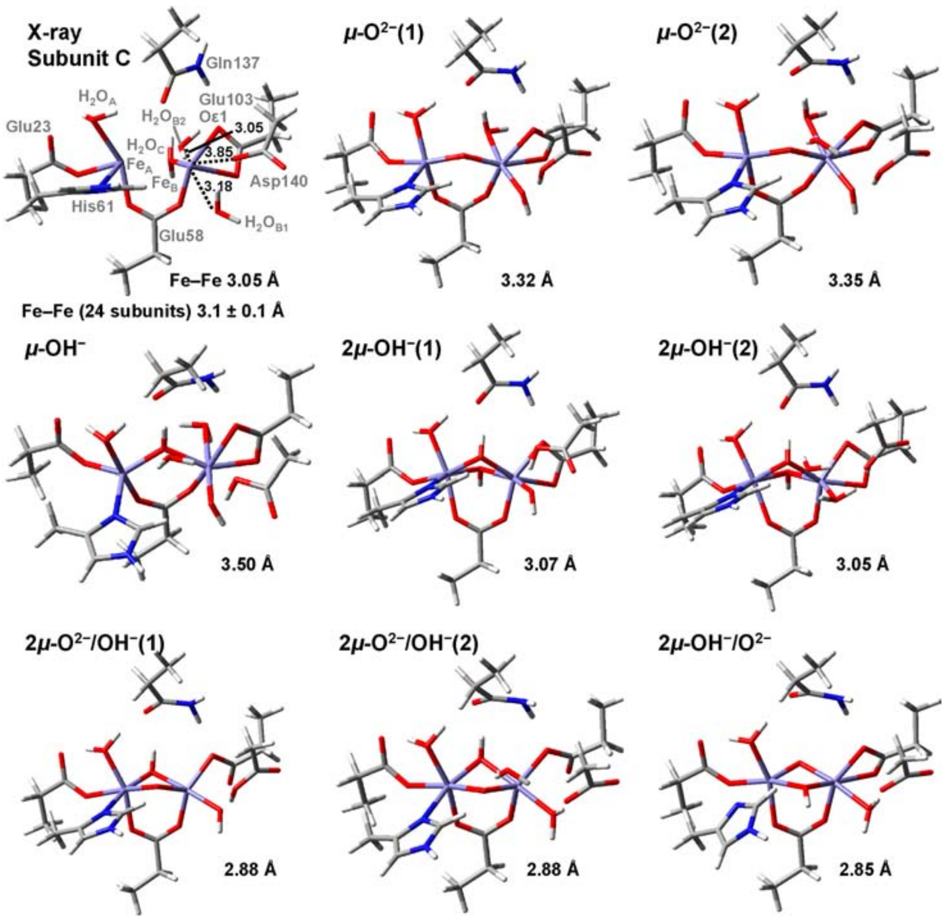

Figure 5. QM/MM-optimized di-Fe(III) models and initial crystallographic structure, including metal−metal distances. Only the QM layer is shown.

corresponding experimental transition. Similar corrections for systematic error have been applied previously for TD-DFT-based CD calculations.[75]

3.2. Structural Models of the Di-Fe(III) Site. The di-Fe(III) site models are based on the 2.7 Å resolution X-ray crystal structure of Fe(III)-bound frog M ferritin.[9] As with the Cu(II)-bound structure used to construct di-Fe(II) site models, the 24 subunits were refined independently, and it was necessary to select one of them to be the basis of the computational model. For this purpose, the rmsd of several critical distances (Fe_A−Glu23(Oε1), −Glu23(Oε2), −Glu58-(Oε1), −His61(Nδ1); Fe_B−Glu58(Oε2), −His54(Nε2), −Glu103(Oε1), −Glu103(Oε2); and $Fe_A \cdots Fe_B$) relative to their respective averages was calculated for each subunit. Subunit C was chosen as it had the lowest rmsd (0.06 Å) and was therefore an approximately average structure.

The di-Fe(III) site had a short Fe−Fe distance of 3.05 Å in subunit C that suggested the presence of a bridging oxo or hydroxo ligand obscured by the electron density of the iron centers. Four waters were resolved in the vicinity, indicated here according to the orientation shown in Figure 5: one above Fe_A (H_2O_A: 2.46 Å), two in front of Fe_B (H_2O_{B1}, 3.18; H_2O_{B2}, 3.05 Å), and one that may be a second bridging ligand, as it is located behind and between Fe_A and Fe_B (H_2O_C: 2.81 and 2.63 Å, respectively). At 2.7 Å resolution, the quantity, composition, and orientation of water-derived species is highly uncertain, and there may be considerable fluctuation around Fe_B, as it is exposed to the solvent-filled cavity. Models for the di-Fe(III) ferroxidase reaction products were constructed by adding a bridging oxo or hydroxo ligand, and the H_2O_C species was modeled as an aqua or hydroxo ($OH^-{}_C$) group. Each structure was also optimized with one or two H_2O_B. The optimizations led to four groups of structures, shown in Figure 5, that can be categorized by the nature of the bridging ligand(s): (1) single μ-hydroxo, (2) single μ-oxo, (3) double μ-hydroxo, or (4) double μ-oxo/hydroxo. Doubly μ-oxo-bridged models were not pursued because the Fe−Fe distances of the double mixed-bridge models are already significantly shorter than the experimental distance, and coordination of His61 is lost when a μ-oxo group is in the *trans* position, as discussed below.

3.2.1. Singly Bridged Models. Singly bridged structures are obtained when H_2O_C is not deprotonated, as it migrates toward Fe_B from its crystallographic position between the two iron centers, instead of acting as a second bridging ligand. The μ-hydroxo-bridged model **μ-OH$^-$** (Figure 5) has a long Fe−Fe distance of 3.50 Å, compared with the experimental distances of 3.1 ± 0.1 (X-ray crystallography)[9] and 2.99 Å (EXAFS),[10] rendering it an unlikely candidate. With the stronger μ-oxo bridge of model **μ-O^{2-}(2)**, the distance decreases to 3.35 Å. Further reduction to 3.32 Å is observed for model **μ-O^{2-}(1)**, which lacks H_2O_{B1} and its hydrogen bond to the μ-oxo group that weakens the bridging bonds in **μ-O^{2-}(2)**. The 3.32 Å Fe−Fe distance is still long, but the square pyramidal Fe_A is open for an additional bridging ligand. Fe_B has a distorted octahedral geometry with bidentate Glu103, and H_2O_{B1} is deprotonated by Asp140, resulting in a bound hydroxo ($OH^-{}_{B1}$) group.

3.2.2. Doubly Bridged Models. When H_2O_C is modeled as a hydroxo group (OH_C), minima are found with it occupying a

Table 3. Calculated and Experimental Mössbauer Parameters and Fe−Fe Distances for Di-Fe(III) Products

model	Fe−Fe	$\delta(\mathrm{Fe_A})$	$\delta(\mathrm{Fe_B})$	$\lvert\Delta E_Q(\mathrm{Fe_A})\rvert$	$\lvert\Delta E_Q(\mathrm{Fe_B})\rvert$
μ-OH$^-$	3.50	0.50	0.50	0.43	1.12
μ-O^{2-}(1)	3.32	0.51	0.50	1.95	1.56
μ-O^{2-}(2)	3.35	0.51	0.50	1.77	1.43
2μ-OH$^-$(1)	3.07	0.56	0.51	0.49	1.25
2μ-OH$^-$(2)	3.05	0.56	0.52	0.23	0.97
2μ-O^{2-}/OH$^-$(1)	2.88	0.54	0.47	1.25	1.23
2μ-O^{2-}/OH$^-$(2)	2.88	0.55	0.47	1.33	0.94
2μ-OH$^-$/O^{2-}	2.85	0.57	0.51	1.21	1.26
exp(1)[a]		0.48		1.95	
exp(2)[a]		0.55		1.63	
exp(3)[a]		0.48		1.17	
exp(4)[a]		0.52		0.63	
crystallography[9]	3.1 ± 0.1				
EXAFS[10]	2.99−3.00[b]				

[a] 1−4 in parentheses refer to the four quadrupole doublets used to fit the experimental[19] spectrum. They are not assigned specifically to $\mathrm{Fe_A}$ or $\mathrm{Fe_B}$.
[b] 2.99 and 3.00 Å were found using two independent samples.

second bridging position, shown in Figure 5. The models with double hydroxo bridges and one (**2μ-OH$^-$(1)**) or two $\mathrm{H_2O_B}$ (**2μ-OH$^-$(2)**) have experimentally consistent Fe−Fe distances of 3.07 and 3.05 Å, respectively. The major difference between the two models is that the additional $\mathrm{H_2O_B}$ of **2μ-OH$^-$(2)** ($\mathrm{H_2O_{B2}}$) is hydrogen bonded to Asp140, preventing deprotonation of $\mathrm{H_2O_{B1}}$. Another set of doubly bridged models can be obtained by substitution of a μ-oxo bridge for the μ-hydroxo bridge in the front position (**2μ-O^{2-}/OH$^-$(1)** and **2μ-O^{2-}/OH$^-$(2)**) or for $\mathrm{OH_C}$ in the back position (**2μ-OH$^-$/O^{2-}**). As expected on the basis of the structures of the doubly hydroxo-bridged models, **2μ-O^{2-}/OH$^-$(1)** and **2μ-O^{2-}/OH$^-$(2)** have overly contracted Fe−Fe distances of 2.88 Å. $\mathrm{H_2O_{B2}}$ in **2μ-O^{2-}/OH$^-$(2)** again forms the hydrogen bond with Asp140 that prevents deprotonation of $\mathrm{H_2O_{B1}}$ in a structure that is otherwise very similar to **2μ-O^{2-}/OH$^-$(1)**. Comparison of these structures to **2μ-OH$^-$/O^{2-}**, which has switched bridging ligand positions, highlights the strong *trans* effect of the oxo bridge. In **2μ-O^{2-}/OH$^-$(1)** and **2μ-O^{2-}/OH$^-$(2)**, Glu103 becomes monodentate as coordination in the *trans* position (Oε2) is lost, whereas in **2μ-OH$^-$/O^{2-}**, His61 occupies the *trans* position and its bond with $\mathrm{Fe_A}$ is broken. The lack of His61 coordination is inconsistent with the crystal structure, but this model could represent a later intermediate in the mineralization pathway, according to the hypothesis of di-Fe(III) product migration.

3.2.3. Mössbauer Isomer Shifts and Quadrupole Splittings.

^{57}Fe Mössbauer spectroscopy provides information about the nature of the ligands and coordination environment and can be used together with the structural parameters derived from crystallography and EXAFS to give a more complete description of the di-Fe(III) products. The 4.2 K Mössbauer spectrum taken 1 s after addition of 36 Fe^{2+}/24 subunits of apo frog M ferritin was broad, and the fitting analysis required at least four quadrupole doublets, indicating variable ligand environments of the products.[19] The Mössbauer parameters (Table 3) were consistent with high-spin Fe(III) centers, and the range of quadrupole splittings (ΔE_Q) (−1.95 to +0.63 mm/s) spanned the typical values (ignoring the sign) of μ-hydroxo- (1.4−2.4 mm/s) and μ-oxo-bridged (0.6−1.0 mm/s) species.

To gain more insight into the structures that gave rise to the various quadrupole doublets and identify products of the ferroxidase reaction, we calculated the isomer shifts (δ) and quadrupole splittings of each of our Fe(III) models. We present only absolute values of the quadrupole splittings in Table 3 because the calculated signs are not always reliable.[65] Quadrupole splittings are sensitive to the charge distribution around the nucleus and are expected to be more strongly influenced by the electrostatic field of the protein environment than are the isomer shifts; thus, the ONIOM-EE method that accounts for polarization of the QM part by the charges of the MM part was used to calculate ΔE_Q. The electrostatic effect turned out to be rather small, perturbing ΔE_Q by, at most, 0.21 mm/s relative to the values calculated using mechanical embedding (ONIOM-ME) without polarization of the QM part. Importantly, the calculated Mössbauer parameters vary between the two sites of most models because of asymmetric coordination environments. **μ-OH$^-$** has two equivalent isomer shifts (0.50 mm/s), but the quadrupole splittings are much different (0.43 and 1.12 mm/s). On the other hand, the doubly bridged models do not all have differing quadrupole splittings for the two sites, but the $\mathrm{Fe_A}$ isomer shifts are all higher (by 0.04−0.08 mm/s) than those of $\mathrm{Fe_B}$. Only the μ-oxo bridged models have similar Mössbauer parameters for the two sites. The conclusion here is that the four experimental quadrupole doublets may represent individual sites, rather than four di-Fe(III) products with equivalent sites.

Table 3 shows that models with various bridging ligands have distinct sets of Mössbauer parameters that differ by as much as 0.07 mm/s in δ, and more than 1 mm/s in ΔE_Q. By contrast, the additional hydrogen bonds and changes in protonation state of the $\mathrm{H_2O_{B1}}$ ligand due to the additional water in models denoted (**2**) cause only small perturbations of ~0.01 mm/s in δ and 0.3 mm/s or less in ΔE_Q. Thus, the experimental quadrupole doublets (Table 3, exp(1−4)) can be attributed to species with different bridging ligands. Exp(1) has the highest absolute value of the quadrupole splitting of 1.95 mm/s that is only approached by the **μ-O^{2-}** models, and the best agreement is found for **μ-O^{2-}(1)** ($\lvert\Delta E_Q(\mathrm{Fe_{A/B}})\rvert$: 1.95/1.56 mm/s); the isomer shifts ($\delta_{A/B}$: 0.51/0.50 mm/s) are also close to the experimental value (0.48 mm/s). Exp(2) has the next highest $\lvert\Delta E_Q\rvert$ value of 1.63 mm/s, and the highest isomer shift of 0.55 mm/s, which is most consistent with the $\mathrm{Fe_A}$ site of **2μ-O^{2-}/OH$^-$(2)** ($\lvert\Delta E_Q\rvert/\delta$: 1.33/0.55 mm/s). The Mössbauer parameters of the $\mathrm{Fe_B}$ site of the same model are significantly different ($\lvert\Delta E_Q(\mathrm{Fe_B})\rvert/\delta(\mathrm{Fe_B})$: 0.94/0.47 mm/s), but they are consistent with those of exp(3) ($|\Delta E_Q|/\delta$: 1.17/0.48 mm/s). Exp(4) remains to be assigned, and it has a low $|\Delta E_Q|$ value (0.63 mm/s) that is similar to that of the Fe_A site of $\mathbf{2\mu\text{-}OH^-(1)}$ ($|\Delta E_Q(Fe_A)|$: 0.49 mm/s). The isomer shift of exp(4) (0.52 mm/s) is not as well reproduced ($\mathbf{2\mu\text{-}OH^-(1)}$ $\delta(Fe_A)$: 0.56 mm/s) as those of the other experimental quadrupole doublets, but consideration of the Fe_B site provides an additional argument in favor of this assignment. The $|\Delta E_Q(Fe_B)|$ value of $\mathbf{2\mu\text{-}OH^-(1)}$ (1.25 mm/s) is consistent with the $|\Delta E_Q|$ value of exp(3) (1.17 mm/s), whereas the isomer shift ($\delta(Fe_B)$: 0.51 mm/s) is higher than that of exp(3) (0.48 mm/s). Thus, the two sites of $\mathbf{2\mu\text{-}OH^-(1)}$ have isomer shifts that are 0.04 and 0.03 mm/s higher than the experimental quadrupole doublets to which they were assigned based on the quadrupole splittings. A small systematic error, which is not unlikely for calculated isomer shifts, could cause this discrepancy.

In summary, exp(1) is assigned to a single di-Fe(III) model, $\mathbf{\mu\text{-}O^{2-}(1)}$, whereas exp(2–4) are assigned to individual iron centers of $\mathbf{2\mu\text{-}O^{2-}/OH^-(2)}$ and $\mathbf{2\mu\text{-}OH^-(1)}$. If the three products represented by these models were produced in equal abundance and were the only dimer products, the intensity ratio of the quadrupole doublets would be 2:1:2:1 for exp(1–4). In the experimental analysis, a minimum of four quadrupole doublets was necessary in the fitting procedure, and the intensities were fixed to be equal; thus, the actual number of products (or unique iron centers) and their relative intensities was not determined. The Fe–Fe distances are 3.32, 3.07, and 2.88 Å for $\mathbf{\mu\text{-}O^{2-}(1)}$, $\mathbf{2\mu\text{-}OH^-(1)}$, and $\mathbf{2\mu\text{-}O^{2-}/OH^-(2)}$, respectively, and the experimental distances, 3.1 ± 0.1 Å (crystallography) and 2.99–3.00 Å (EXAFS), are in the middle of this range. The EXAFS results represent an average over the products, whereas in the crystal structure some of the variation in Fe–Fe distances between subunits may be due to the various products. For example, subunits U (3.22 Å), C (3.05 Å), and K (2.89 Å) may be most representative of the μ-oxo-, double μ-hydroxo-, and double μ-oxo/hydroxo-bridged products, respectively. The μ-hydroxo-bridged model can be excluded from consideration due to the long Fe–Fe distance (3.50 Å), and the Mössbauer parameters are less experimentally consistent than those of the other models.

4. CONCLUSIONS

In this ONIOM-based investigation, we have identified the most likely structure of the initial Fe(II)-bound ferroxidase site, and described three di-Fe(III) products that coexist in different subunits. The favored di-Fe(II) model, **R6**, has 5-coordinate iron sites with ligand fields best described as square pyramidal but with distortion toward trigonal bipyramidal geometry. This is reasonable, considering the previous analysis of CD/MCD data that led to the assignment of one square pyramidal and one trigonal bipyramidal site. The Fe–Fe distance of 4.48 Å is well within the experimental range of Cu–Cu distances (4.3 ± 0.4 Å) in the structural analog on which our di-Fe(II) models were based. In general, the Fe–Fe distances are too long in models with bidentate coordination of Glu23 and one aqua ligand at the Fe_A site (H_2O_A). **R6** has monodentate Glu23 and two H_2O_A ligands that are involved in a complex hydrogen-bond network that contributes to the shorter Fe–Fe separation. The calculated exchange coupling constant (J) for **R6** (−0.9 cm^{-1}) is in excellent agreement with the experimental value (−0.8 cm^{-1}), which can be regarded as quantitatively fortuitous, but it is certainly consistent with very weak antiferromagnetic coupling. Similar J values were determined for other models, and the furthest outlier, −2.6 cm^{-1}, was attributed to the weakly μ-aqua-bridged model (**R10**). Comparison of the relative transition energies in the calculated and experimental CD spectra allowed differentiation of the models with reasonable coordination geometries, Fe–Fe distances, and J values, favoring **R6** above all others. In the previous analysis of the experimental CD spectra, the transitions were determined to alternate between iron sites, and on the basis of a Mg(II)-bound ferroxidase site,[11] the 7600/11 150 cm^{-1} pair, typical for a square pyramidal Fe(II) site, was assigned to Fe_A.[16] However, the recent Cu(II)-loaded structure reveals a different coordination environment at Fe_B, including His54, that was previously not considered to be involved, and our optimized models show that Fe_B can have a square pyramidal ligand field. Thus, our calculations favor assigning the 7600/11 150 cm^{-1} pair to Fe_B, as this leads to very good agreement between the splittings of the two transitions attributed to each iron site of **R6–R8** and the experimental splittings.

The di-Fe(III) products were identified on the basis of Fe–Fe distances and Mössbauer parameters. A μ-hydroxo-bridge is too weak, as even with a μ-oxo bridge, the Fe–Fe distances are significantly longer than those derived via crystallography and EXAFS. The best agreement is found for the double μ-hydroxo-bridged models, whereas deprotonating one of the two bridges results in a structure that is overly compact. However, the experimental distances are averaged over multiple products, and it is reasonable to have individual Fe–Fe distances that are long or short. For most models, the Mössbauer parameters differed between Fe_A and Fe_B; thus, the experimental quadrupole doublets were assigned not just to models but also to individual iron sites. The μ-oxo-, double μ-hydroxo-, and double μ-hydroxo/oxo-bridged models all had isomer shifts and quadrupole splittings that were consistent with the experimental values, and it is likely that all three are produced simultaneously in different subunits. In the flexible, partially solvent-exposed ferroxidase site, there must be considerable variation in the hydrogen-bond network and protonation states of terminal water-derived ligands and nearby residues, but we found that such factors only result in small perturbations to the Mössbauer spectra. Hence, the distinct experimental quadrupole doublets must be attributed to major structural differences, such as different bridging ligands.

In comparing the structures of the best di-Fe(II) model, **R6**, and the three di-Fe(III) products, $\mathbf{\mu\text{-}O^{2-}(1)}$, $\mathbf{2\mu\text{-}OH^-(1)}$, and $\mathbf{2\mu\text{-}O^{2-}/OH^-(2)}$, without considering the bridging ligands of the products, we see very similar Fe_A sites but substantial variation at the Fe_B site. The only major difference regarding Fe_A is an aqua ligand in **R6** that may be a precursor to the bridging ligand(s) of the products. It may become a bridging ligand already in the peroxo intermediate, which has a very short Fe–Fe distance of 2.53 Å that requires a water-derived bridging ligand. The Fe_B site, however, is very different, as His54 and Asp140 are coordinated in **R6**, but not in the products. One of the coordination positions eventually becomes occupied by a terminal aqua/hydroxo ligand (a proton is transferred to Asp140 in two of the product models). The variable Asp140 coordination is consistent with the experimental findings that an Asp140Ala mutation reduces Fe(II) binding affinity, whereas the peroxo intermediate is not observed in an Asp140His ferritin,[13] as His140 likely prevents Fe_B from migrating close enough to Fe_A to form the peroxo intermediate. Although we did not directly investigate the peroxo intermediate in this study, based on Fe−Fe distances, its structure likely resembles the di-Fe(III) models (shortest Fe−Fe: 2.88 Å) more than **R6**. Glu23, His61, and H_2O are expected to coordinate Fe_A, whereas Fe_B must dissociate from His54 and Asp140 as the Fe−Fe distance closes. Further calculations will be necessary to identify the bridging ligands, but based on the doubly bridged structures presented here, the peroxo and oxo groups may not be sufficient to bring the irons within 2.53 Å. In a previous DFT study, an Fe−Fe distance of 2.65 Å was found for a peroxo- and double μ-oxo-bridged model of the HuHF ferroxidase site without Glu58.[26] The possibility of Glu58 shifting to a μ-1,1 bridging mode, as in methane monooxygenase,[76] should be investigated.

A notable feature that is constant between **R6** and the products is the lack of direct coordination of Gln137. This residue has been considered to be a possible Fe_B ligand,[16] but it has not been close enough to an Fe site to directly coordinate in the available crystal structures. However, it interacts with H_2O_A ligands in the Zn(II)- and Co(II)-bound structures and also with the Glu103 ligand of the B-site Zn(II). In most of our geometry optimizations Gln137 did not coordinate directly, but it was always hydrogen bonded to one or more H_2O_A ligands, Glu103(Oε1), and sometimes H_2O_B or a bridging hydroxo group. As described in Section 3.1.2, the hydrogen-bond network in models such as **R6** reduces the Fe−Fe distance compared with that in **R7**, in which Gln137 has a weaker connection to Fe_A. **R7** has Gln137 bound to Fe_B, and it was the only local minimum that we found and analyzed with Gln137 coordinated to either Fe. The CD spectra and coordination geometries of **R7** are reasonable, but the slightly less experimentally consistent relative transition energies, combined with a large deviation in Gln137 position from that of the crystal structure and a J value (-0.2 cm^{-1}) that is 4-fold weaker than that of **R6** and the experiment, render **R7** a less likely candidate. Thus, the present results demonstrate the role of Gln137 in maintaining the structure of the ferroxidase site through hydrogen bonds with Fe ligands in both the initial Fe(II) and product Fe(III) states. Future mechanistic studies may reveal that it participates in proton transfer steps necessary for decay of the peroxo intermediate, bridge formation, and product release.[19,77]

The structures identified in this work will be the basis of future mechanistic studies. Currently, we are applying the methods used here to identify a spectroscopically consistent structure of the peroxo intermediate. With the key structures in hand, we will be in position to explore the pathway connecting the di-Fe(II) state to the peroxo intermediate and the branching mechanisms that lead to the multiple products found in this work.

■ ASSOCIATED CONTENT

Ⓢ Supporting Information

Table S1, Figures S1 and S2, complete author listing for ref 55, Cartesian coordinates for ONIOM-optimized QM layers of each model. This material is available free of charge via the Internet at http://pubs.acs.org.

■ AUTHOR INFORMATION

Corresponding Author

*E-mail: morokuma@fukui.kyoto-u.ac.jp.

Notes

The authors declare no competing financial interest.

■ ACKNOWLEDGMENTS

T.V.H. thanks Prof. Robert Szilagyi for pointing him toward the remarkable field of ferritin research. We also thank Prof. Kenneth Hardcastle for input regarding how to choose subunits on which to base our models. T.V.H. was supported by a Japan Society for the Promotion of Science (JSPS) Fellowship. The use of computational resources at the Research Center of Computer Science (RCCS) at the Institute for Molecular Science (IMS) is acknowledged.

■ REFERENCES

(1) Arosio, P.; Ingrassia, R.; Cavadini, P. *Biochim. Biophys. Acta* **2009**, *1790* (7), 589−599.

(2) Theil, E. C. *Curr. Opin. Chem. Biol.* **2011**, *15* (2), 304−311.

(3) Bou-Abdallah, F. *Biochim. Biophys. Acta* **2010**, *1800* (8), 719−731.

(4) Liu, X. F.; Theil, E. C. *Acc. Chem. Res.* **2005**, *38* (3), 167−175.

(5) Turano, P.; Lalli, D.; Felli, I. C.; Theil, E. C.; Bertini, I. *Proc. Natl. Acad. Sci. U. S. A.* **2010**, *107* (2), 545−550.

(6) Haldar, S.; Bevers, L. E.; Tosha, T.; Theil, E. C. *J. Biol. Chem.* **2011**, *286* (29), 25620−25627.

(7) Ebrahimi, K. H.; Bill, E.; Hagedoorn, P. L.; Hagen, W. R. *Nat. Chem. Biol.* **2012**, *8* (11), 941−948.

(8) Treffry, A.; Zhao, Z.; Quail, M. A.; Guest, J. R.; Harrison, P. M. *Biochemistry* **1995**, *34* (46), 15204−15213.

(9) Bertini, I.; Lalli, D.; Mangani, S.; Pozzi, C.; Rosa, C.; Theil, E. C.; Turano, P. *J. Am. Chem. Soc.* **2012**, *134* (14), 6169−6176.

(10) Hwang, J.; Krebs, C.; Huynh, B. H.; Edmondson, D. E.; Theil, E. C.; Penner-Hahn, J. E. *Science* **2000**, *287* (5450), 122−125.

(11) Ha, Y.; Shi, D. S.; Small, G. W.; Theil, E. C.; Allewell, N. M. *J. Biol. Inorg. Chem.* **1999**, *4* (3), 243−256.

(12) Toussaint, L.; Bertrand, L.; Hue, L.; Crichton, R. R.; Declercq, J. P. *J. Mol. Biol.* **2007**, *365* (2), 440−452.

(13) Tosha, T.; Hasan, M. R.; Theil, E. C. *Proc. Natl. Acad. Sci. U. S. A.* **2008**, *105* (47), 18182−18187.

(14) Lawson, D. M.; Artymiuk, P. J.; Yewdall, S. J.; Smith, J. M. A.; Livingstone, J. C.; Treffry, A.; Luzzago, A.; Levi, S.; Arosio, P.; Cesareni, G.; Thomas, C. D.; Shaw, W. V.; Harrison, P. M. *Nature* **1991**, *349* (6309), 541−544.

(15) Tosha, T.; Ng, H. L.; Bhattasali, O.; Alber, T.; Theil, E. C. *J. Am. Chem. Soc.* **2010**, *132* (41), 14562−14569.

(16) Schwartz, J. K.; Liu, X. S.; Tosha, T.; Theil, E. C.; Solomon, E. I. *J. Am. Chem. Soc.* **2008**, *130* (29), 9441−9450.

(17) Pereira, A. S.; Small, W.; Krebs, C.; Tavares, P.; Edmondson, D. E.; Theil, E. C.; Huynh, B. H. *Biochemistry* **1998**, *37* (28), 9871−9876.

(18) Moenne-Loccoz, P.; Krebs, C.; Herlihy, K.; Edmondson, D. E.; Theil, E. C.; Huynh, B. H.; Loehr, T. M. *Biochemistry* **1999**, *38* (17), 5290−5295.

(19) Jameson, G. N. L.; Jin, W.; Krebs, C.; Perreira, A. S.; Tavares, P.; Liu, X. F.; Theil, E. C.; Huynh, B. H. *Biochemistry* **2002**, *41* (45), 13435−13443.

(20) Bou-Abdallah, F.; Papaefthymiou, G. C.; Scheswohl, D. M.; Stanga, S. D.; Arosio, P.; Chasteen, N. D. *Biochem. J.* **2002**, *364*, 57−63.

(21) Krebs, C.; Bollinger, J. M.; Theil, E. C.; Huynh, B. H. *J. Biol. Inorg. Chem.* **2002**, *7* (7−8), 863−869.

(22) Bauminger, E. R.; Harrison, P. M.; Hechel, D.; Hodson, N. W.; Nowik, I.; Treffry, A.; Yewdall, S. J. *Biochem. J.* **1993**, *296*, 709−719.

(23) Bacelo, D. E.; Binning, R. C. *J. Phys. Chem. A* **2009**, *113* (7), 1189−1198.

(24) Binning, R. C.; Bacelo, D. E. *J. Biol. Inorg. Chem.* **2009**, *14* (8), 1199−1208.

(25) Bacelo, D. E.; Binning, R. C. *Chem. Phys. Lett.* **2011**, *507* (1−3), 174−177.

(26) Bacelo, D. E.; Binning, R. C. *Inorg. Chem.* **2006**, *45* (25), 10263−10269.

(27) Laghaei, R.; Evans, D. G.; Coalson, R. D. *Proteins: Struct., Funct., Bioinf.* **2013**, *81* (6), 1042−1050.

(28) Subramanian, V.; Evans, D. G. *J. Phys. Chem. B* **2012**, *116* (31), 9287−9302.

(29) Ciacchi, L. C.; Payne, M. C. *Chem. Phys. Lett.* **2004**, *390* (4−6), 491−495.

(30) Ke, Z. F.; Abe, S.; Ueno, T.; Morokuma, K. *J. Am. Chem. Soc.* **2012**, *134* (37), 15418−15429.

(31) Humphrey, W.; Dalke, A.; Schulten, K. *J. Mol. Graphics Modell.* **1996**, *14* (1), 33−38.

(32) Cornell, W. D.; Cieplak, P.; Bayly, C. I.; Gould, I. R.; Merz, K. M.; Ferguson, D. M.; Spellmeyer, D. C.; Fox, T.; Caldwell, J. W.; Kollman, P. A. *J. Am. Chem. Soc.* **1995**, *117* (19), 5179−5197.

(33) Phillips, J. C.; Braun, R.; Wang, W.; Gumbart, J.; Tajkhorshid, E.; Villa, E.; Chipot, C.; Skeel, R. D.; Kale, L.; Schulten, K. *J. Comput. Chem.* **2005**, *26* (16), 1781−1802.

(34) Levi, S.; Santambrogio, P.; Albertini, A.; Arosio, P. *FEBS Letters* **1993**, *336* (2), 309−312.

(35) Huard, D. J. E.; Kane, K. M.; Tezcan, F. A. *Nat. Chem. Biol.* **2013**, *9* (3), 169−176.

(36) Maseras, F.; Morokuma, K. *J. Comput. Chem.* **1995**, *16* (9), 1170−1179.

(37) Svensson, M.; Humbel, S.; Froese, R. D. J.; Matsubara, T.; Sieber, S.; Morokuma, K. *J. Phys. Chem.* **1996**, *100* (50), 19357−19363.

(38) Dapprich, S.; Komaromi, I.; Byun, K. S.; Morokuma, K.; Frisch, M. J. *THEOCHEM.* **1999**, *461*, 1−21.

(39) Vreven, T.; Byun, K. S.; Komaromi, I.; Dapprich, S.; Montgomery, J. A.; Morokuma, K.; Frisch, M. J. *J. Chem. Theory Comput.* **2006**, *2* (3), 815−826.

(40) Becke, A. D. *Phys. Rev. A* **1988**, *38* (6), 3098−3100.

(41) Vosko, S. H.; Wilk, L.; Nusair, M. *Can. J. Phys.* **1980**, *58* (8), 1200−1211.

(42) Lee, C. T.; Yang, W. T.; Parr, R. G. *Phys. Rev. B* **1988**, *37* (2), 785−789.

(43) Hoffmann, M.; Khavrutskii, I. V.; Musaev, D. G.; Morokuma, K. *Int. J. Quantum Chem.* **2004**, *99* (6), 972−980.

(44) Hirao, H.; Morokuma, K. *J. Am. Chem. Soc.* **2009**, *131* (47), 17206−17214.

(45) Noodleman, L. *J. Chem. Phys.* **1981**, *74* (10), 5737−5743.

(46) Wedig, U.; Dolg, M.; Stoll, H.; Preuss, H. In *Quantum Chemistry: The Challenge of Transition Metals and Coordination Chemistry*; Veillard, A., Ed.; Reidel: Dordrecht, The Netherlands, 1986; pp 79−90.

(47) Dolg, M.; Wedig, U.; Stoll, H.; Preuss, H. *J. Chem. Phys.* **1987**, *86* (2), 866−872.

(48) Hehre, W. J.; Ditchfie., R.; Pople, J. A. *J. Chem. Phys.* **1972**, *56* (5), 2257−&.

(49) Hehre, W. J.; Random, L.; Schleyer, P. v. R.; Pople, J. A. *Ab Initio Molecular Orbital Theory*; Wiley: New York, 1986.

(50) Hariharan, P. C.; Pople, J. A. *Theor. Chim. Acta* **1973**, *28* (3), 213−222.

(51) Francl, M. M.; Pietro, W. J.; Hehre, W. J.; Binkley, J. S.; Gordon, M. S.; Defrees, D. J.; Pople, J. A. *J. Chem. Phys.* **1982**, *77* (7), 3654−3665.

(52) M−L bond distances of the di-Fe(II) model **R6** optimized using the larger basis set deviated by, at most, 0.02 Å, with the exception of one Fe_A-H_2O bond (2.35/2.30 Å for def-TZVP/SDD) and the Fe_B−Glu103(Oε1) interaction (2.68/2.53 Å), but these are the weakest bonds with the flattest potential energy surfaces, and it is not unexpected to see larger deviations. The Fe−Fe distance of 4.52 Å was only 0.04 Å longer than with the smaller basis set. CD transitions from a subsequent TD-DFT calculation using the def-TZVP structure were within ~350 cm^{-1} of those based on the SDD/6-31G(d) structure, and there were no significant variations in rotatory strength; thus, the employed structures are adequate. A di-Fe(III) model, **μ-O^{2-}(1)**, was also optimized with def-TZVP and the deviations were small: all M−L bonds were within 0.01 Å and the Fe−Fe distance (3.35 Å) was 0.03 Å longer.

(53) Singh, U. C.; Kollman, P. A. *J. Comput. Chem.* **1984**, *5* (2), 129−145.

(54) Besler, B. H.; Merz, K. M.; Kollman, P. A. *J. Comput. Chem.* **1990**, *11* (4), 431−439.

(55) Frisch, M. J.; et al. *Gaussian 09*, Rev C.01; Gaussian, Inc: Wallingford, CT, 2011.

(56) Tao, P.; Schlegel, H. B. *J. Comput. Chem.* **2010**, *31* (12), 2363−2369.

(57) Weigend, F.; Ahlrichs, R. *Phys. Chem. Chem. Phys.* **2005**, *7* (18), 3297−3305.

(58) Schafer, A.; Horn, H.; Ahlrichs, R. *J. Chem. Phys.* **1992**, *97* (4), 2571−2577.

(59) Schafer, A.; Huber, C.; Ahlrichs, R. *J. Chem. Phys.* **1994**, *100* (8), 5829−5835.

(60) O'Boyle, N. M.; Tenderholt, A. L.; Langner, K. M. *J. Comput. Chem.* **2008**, *29* (5), 839−845.

(61) Martin, R. L. *J. Chem. Phys.* **2003**, *118* (11), 4775−4777.

(62) Wachters, A. J. *J. Chem. Phys.* **1970**, *52* (3), 1033.

(63) Dunning, T. H. *J. Chem. Phys.* **1989**, *90* (2), 1007−1023.

(64) Keith, T. A. *AIMAll*, Version 12.05.09; TK Gristmill Software: Overland Park, KS, 2012; aim.tkgristmill.com.

(65) Bochevarov, A. D.; Friesner, R. A.; Lippard, S. J. *J. Chem. Theory Comput.* **2010**, *6* (12), 3735−3749.

(66) Sinnecker, S.; Slep, L. D.; Bill, E.; Neese, F. *Inorg. Chem.* **2005**, *44* (7), 2245−2254.

(67) Soda, T.; Kitagawa, Y.; Onishi, T.; Takano, Y.; Shigeta, Y.; Nagao, H.; Yoshioka, Y.; Yamaguchi, K. *Chem. Phys. Lett.* **2000**, *319* (3−4), 223−230.

(68) Ruiz, E. *Struct. Bonding (Berlin, Ger.)* **2004**, *113*, 71.

(69) Reem, R. C.; Solomon, E. I. *J. Am. Chem. Soc.* **1987**, *109* (4), 1216−1226.

(70) Hagen, K. S.; Lachicotte, R. *J. Am. Chem. Soc.* **1992**, *114* (22), 8741−8742.

(71) Brunold, T. C.; Solomon, E. I. *J. Am. Chem. Soc.* **1999**, *121* (36), 8277−8287.

(72) Solomon, E. I.; Pavel, E. G.; Loeb, K. E.; Campochiaro, C. *Coord. Chem. Rev.* **1995**, *144*, 369−460.

(73) Srnec, M.; Rokob, T. A.; Schwartz, J. K.; Kwak, Y.; Rulisek, L.; Solomon, E. I. *Inorg. Chem.* **2012**, *51* (5), 2806−2820.

(74) The Fe_A-based roots of **R11** are 4 and 8, giving a very large 6885 cm^{-1} splitting and three consecutive Fe_B-site transitions, which are not consistent with the experiment.

(75) Autschbach, J.; Ziegler, T.; van Gisbergen, S. J. A.; Baerends, E. J. *J. Chem. Phys.* **2002**, *116* (16), 6930−6940.

(76) Torrent, M.; Musaev, D. G.; Morokuma, K. *J. Phys. Chem. B* **2001**, *105* (1), 322−327.

(77) Bou-Abdallah, F.; Zhao, G. H.; Mayne, H. R.; Arosio, P.; Chasteen, N. D. *J. Am. Chem. Soc.* **2005**, *127* (11), 3885−3893.